DOI: 10.1478/AAPP.981A5

AAPP | Atti della Accademia Peloritana dei Pericolanti
Classe di Scienze Fisiche, Matematiche e Naturali
ISSN 1825-1242

Vol. 98, No. 1, A5 (2020)

MONTE CARLO BASED DOSE-RATE ASSESSMENT IN ^{18}F-CHOLINE PET EXAMINATION: A COMPARISON BETWEEN GATE AND GAMOS CODES

DANIELE PISTONE [ab], LUCREZIA AUDITORE [c], ANTONIO ITALIANO [ab*], GIUSEPPE MANDAGLIO [ab], FABIO MINUTOLI [cd], SERGIO BALDARI [cd], AND ERNESTO AMATO [bc]

ABSTRACT. Monte Carlo simulation of radiation transport is the most accurate and patient-specific technique available for internal dosimetry in nuclear medicine. Taking morphological and functional information from CT and PET 3D scans, it is possible to perform MC dose calculations at voxel level. GATE and GAMOS are among the most used and validated toolkits developed for performing such medical physics calculations. Aim of this work was the comparison of dose rates evaluated by means of GATE and GAMOS simulations for a case of PET/CT diagnostic exam conducted with ^{18}F-choline radiopharmaceutical. The results obtained with the two toolkits showed a good agreement, with just some minor differences imputable to their different procedure of voxel density assignment. A further investigation on spurious decays generated in air was conducted through simulations employing a PET-filtering technique. In this way it was highlighted the effect of PET background on the evaluation of dose rates imparted to air-rich organs, in particular lungs.

1. Introduction

Internal dosimetry in nuclear medicine aims at estimating the radiation absorbed doses to tissues and organs during diagnostic and therapeutic procedures employing radiopharmaceuticals. It plays a fundamental role in radiation protection for PET and SPECT exams and in receptorial and metabolic radiotherapy planning and monitoring (Stokke *et al.* 2017).

Three dimensional internal dosimetry calculations can be carried out at whole-organ level, using simplified geometries and assuming uniform activity distribution within each source organ, or at voxel level, considering tissue regions with dimensions in the range from few centimeters to tenths of millimeters. The main voxel dosimetry approaches are the convolution of dose point-kernels (Giap *et al.* 1995), the voxel S values (VSVs) approach (Bolch *et al.* 1999; Amato *et al.* 2012, 2013a,b) and the direct Monte Carlo (MC) simulation of radiation transport (Amato *et al.* 2018; Auditore *et al.* 2019). Direct MC coupled with functional and anatomical imaging is considered the most accurate and patient-specific method for dose estimation (Dewaraja *et al.* 2012), allowing in particular higher precision

TABLE 1. Resolution and voxel dimension for the CT and PET scans used as input data; the administered activity to the patient, $A(t_0)$, and the interval of time between the administration and the scan acquisition, Δt, are also reported for the PET scan.

CT	resolution	$256 \times 256 \times 520$
	voxel dimension (mm)	$2.34 \times 2.34 \times 2.00$
PET	radiotracer	^{18}F-choline
	$A(t_0)$ (MBq)	296
	Δt (min.)	84
	resolution	$144 \times 144 \times 255$
	voxel dimension (mm)	$4.00 \times 4.00 \times 4.00$

in dealing with the actual tissue inhomogeneities and activity nonuniformities (Auditore *et al.* 2019), at the expense of a longer computational time.

Among the software packages developed for the simulation of radiation interaction and transport in matter, Geant4 (Agostinelli *et al.* 2003) is one of the most validated and widely used, notably for medical physics purposes (Allison *et al.* 2016). GATE (Geant4 Application for Emission Tomography) (Jan *et al.* 2004) is a toolkit that offers a user-friendly interface for Geant4, specific for emission tomography and suited for dose calculations in radiotherapy and nuclear medicine applications (Sarrut *et al.* 2014). Another powerful and versatile simulation toolkit for medical physics applications is GAMOS (Geant4-based Architecture for Medicine-Oriented Simulations) (Arce *et al.* 2008), likewise based on Geant4 and providing another easy-to-use framework to simulate projects without C++ coding.

Aim of this work was the comparison and quantitative agreement analysis of dose rates assessed in main organs obtained from GATE and GAMOS Monte Carlo simulation based on the same ^{18}F-Choline PET/CT patient data.

2. Materials and methods

The present comparative study of GATE and GAMOS codes applied to PET internal voxel dosimetry was conducted using input data from a diagnostic ^{18}F-Choline PET/CT. The PET/CT scan was performed with the Philips Gemini TF 16 scanner at the Nuclear Medicine Unit of the University Hospital "G. Martino" in Messina (Italy). Relevant acquisition parameters are reported in Table 1. The original CT scan examined was composed of 1019 slices with axial resolution of 512×512, providing voxel dimensions of $(1.17 \times 1.17 \times 1.00)$ mm^3. In order to shorten the simulation time, we resampled images by means of the *Resample Scalar Volume* module of the software 3DSlicer (2020), via linear interpolation, doubling the voxel size dimensions to get the resolution reported in Table 1. ^{18}F-choline employs ^{18}F as a radioactive marker, a positron emitting isotope of fluorine widely used in PET practice, characterized by a $T_{1/2} = 110$' and $\langle E_{\beta^+} \rangle = 0.63$ MeV (Jacobson *et al.* 2015). Choline is a precursor for the biosynthesis of phospholipids, which are major components of the cellular membrane. Radiolabeled choline allows to detect tumors,

TABLE 2. HU intervals and corresponding density ρ intervals for the materials Geant4 (2020) used in the simulations.

Material	**HU intervals**	$\boldsymbol{\rho}$ **(g/cm^3)**
G4_AIR	HU $\leq$ -855.75	$\rho \leq 0.10$
G4_LUNG_ICRP	-855.75 $<$ HU $\leq$ -126.50	$0.10 < \rho \leq 0.85$
G4_ADIPOSE_TISSUE_ICRP	-126.50 $<$ HU $\leq$ -38.98	$0.85 < \rho \leq 0.94$
G4_TISSUE_SOFT_ICRP	-38.98 $<$ HU $\leq$ 343.61	$0.94 < \rho \leq 1.2$
G4_BONE_CORTICAL_ICRP	HU $>$ 343.61	$\rho > 1.2$

TABLE 3. HU-to-density calibration values for the scanner used.

HU	-1000	-700	-450	0	300	1000	1400	2500	3500
$\boldsymbol{\rho}$ **(g/cm^3)**	0.0012	0.187	0.521	1.0	1.169	1.594	1.837	2.506	3.113

especially prostate cancer, because of the enhanced choline uptake due to the pathologic increased demand for cellular membrane synthesis (Jadvar 2012). Therefore ^{18}F-choline PET/CT is used in the diagnosis and staging of prostate cancer.

Our Monte Carlo simulations were carried out using GATE version 8.1, that relies on Geant4 version 10.04.p03, and GAMOS version 6.0.0, that relies on Geant4 10.02. Both GATE and GAMOS allow using CT images in DICOM format to define a voxelized phantom reproducing patient morphology, and PET images in DICOM format to define a voxelized source decay event probability distribution, derived from the PET voxelized activity concentration distribution. The decay of radioactive nuclei constituting the emitting source, in our case ^{18}F, was simulated in both toolkits using *G4RadioactiveDecay* Geant4 module and associated classes (Geant4 2020). To account for all possible electromagnetic interactions in the simulations, the Geant4 physics list *G4EmStandardPhysics_option3* was used (Geant4 2020). In order to accurately sample the spatial distribution of energy deposition, we set, for the propagation of all the simulated particles and radiation, a lower range cut of 50 μm, significantly shorter than the voxel dimension, that for electrons in soft tissue corresponds to an energy cut of about 15 keV.

2.1. GATE. CT DICOM images were imported to generate a voxelized phantom volume through the *ImageNestedParametrisedVolume* algorithm GATE (2020). Materials were assigned to each voxel of the phantom based on its corresponding Hounsfield Unit (HU) value in the CT, by means of automated HU stoichiometric calibration. In order to identify the materials and their chemical composition (taken from the database Geant4 2020), five intervals of HU were associated to five intervals of mass density, corresponding to the materials to be assigned (namely: air, lung, adipose, soft and cortical bone tissues) as reported in Table 2, by applying a scanner-specific bi-linear relation reported in Table 3 and displayed in Fig. 1. The number and type of materials were properly chosen to mimic the density inhomogeneities in the thoraco-abdominal districts of the human body.

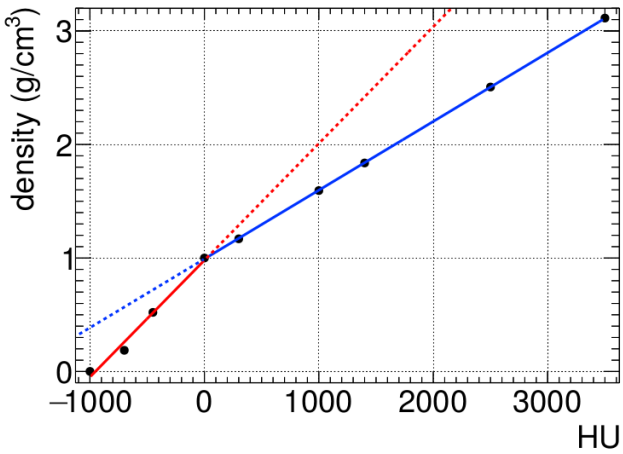

FIGURE 1. HU-to-density calibration points and their bi-linear fit.

The automated calibration defines a set of "sub-materials" for each of the aforementioned materials. Each sub-material has the same chemical composition of the material from which is generated. To each sub-material a different density is assigned, through the interpolation of the HU-density calibration points seen above in Table 3 and Fig. 1; sub-materials are generated having densities differing for less than a density tolerance value (GATE 2020), that we set 0.1 g/cm^3. To each voxel is therefore assigned one of these sub-materials, thus a proper chemical composition and density.

PET DICOM images were imported as a voxelized source volume, and to each voxel was assigned an event generation probability through a linear conversion of its PET value (in the present case activity concentration, expressed in Bq/mL). Voxelized phantom and source volumes were placed in the GATE spatial reference system applying the adequate spatial translations in order to have the correct relative position, according to the information reported in the DICOM file headers. Physics (decays and interactions) was simulated as previously stated, with ^{18}F treated as a GATE ion type source for simulating its decay. The absorbed doses and their statistical uncertainties were scored at voxel level with GATE's *DoseActor*, using the *MassWeighting* algorithm (GATE 2020); the "dosel" grid (*i.e.*, the voxelized dose map) adopted the same spatial dimensions of the input phantom matrix. The simulation used a Mersenne Twister random number generator.

2.2. GAMOS. GAMOS converts CT DICOM images into a logical voxelized phantom volume and permits to directly set voxel-specific densities through the bi-linear calibration with HU yet seen in Table 3 and Fig. 1. Then five intervals of density (Table 2) identify the different chemical compositions of materials, which are the same ones chosen for the GATE simulations.

For reproducing the radionuclide distribution, PET data were used to model a source volume in linear relationship with its activity concentration values, employing the generator class *GmGenerDistPositionInVoxelsFromFile* (GAMOS 2020). Phantom and source were

placed in GAMOS reference system according to the position information included in the DICOM header, and physics was simulated with the Geant4 modules previously described. As done for GATE simulations, the dosel grid volume was defined with the same dimensions of the input phantom matrix, using GAMOS *GmPSPrinter3ddose* scorer (GAMOS 2020).

From MC outputs we obtained 3D absorbed dose maps, from which, dividing each dose voxel for the total number of generated events in the simulation, we deduced dose-per-event maps. Multiplying each dose-per-event voxel by the whole body total activity at the PET scan acquisition time $t = t_s$, we calculated dose rate maps at the acquisition time. Therefore, indicating with D_{ijk} (Gy) the absorbed dose in the field-of-view (FOV) associated to a given voxel (i, j, k), with N_{evts} the total number of generated events employed in the simulation and with $A(t_s)$ (MBq) the total activity measured in the PET field-of-view at the acqusition time, the dose rate $\dot{D}_{ijk}(t_s)$ (Gy $\cdot$ s^{-1}) at the acquisition time in the FOV associated to a given voxel (i, j, k) is expressed and calculated as:

$$\dot{D}_{ijk}(t_s) = \frac{D_{ijk}}{N_{evts}} \cdot A(t_s) \tag{1}$$

$A(t_s)$ was deduced from the PET image and its related informations, applying the adequate factors as follows:

$$\begin{aligned} A(t_s) = \sum_{ijk} A_{ijk}(t_s) &= \langle A_{ijk}(t_s) \rangle \cdot N_{voxels} = \\ &= \langle c_{ijk}(t_s) \rangle \cdot V_{voxel} \cdot N_{voxels} \end{aligned} \tag{2}$$

where N_{voxels} is the total number of voxels in the PET image, $\langle A_{ijk}(t_s) \rangle$ (MBq) is the mean value of the activity in a single PET voxel at the acquisition time, $\langle c_{ijk}(t_s) \rangle$ (MBq/mm^3) is the mean value of the activity concentration in a single PET voxel at the acquisition time, V_{voxel} (mm^3) is the volume of the PET voxel. All the mathematical operations on voxelized images were performed with 3DSlicer.

Furthermore, we used the dose rate maps to evaluate dose rate average values in selected Volumes of Interest (VOIs) and to build Dose Rate Volume Histograms (DRVHs in the following) in the VOIs. From literature it is known that liver is among the organs with the highest ^{18}F-choline uptake following from the normal choline biodistribution (Jadvar 2012), and that can be seen also for the present case in the PET scan (a coronal PET slice fused with the corresponding co-registered CT slice is shown in Fig. 2(a)). Consequently liver, as a source organ for radiation dosimetry, is expected to exhibit one of the highest dose rates at the moment of the PET/CT acquisition. Lungs, especially the right one, above the liver, will also be characterized by non-negligible dose rates. Using 3DSlicer *Segmentation* module we segmented three VOIs on the CT images, corresponding to the following organs: liver, right lung, left lung (whose contours are shown in Fig. 2(a) superimposed to the PET/CT image). Dose rate average values in VOIs and DRVHs were computed using 3DSlicer *Segment Statistics* and *Dose Volume Histogram* modules respectively.

2.3. Background and artifacts treatment. On the basis of the preliminary results obtained during our study, we decided to investigate the influence of background present into the PET image, used as input data, on the dose rate outcomes obtained through MC simulation. In the present work we aimed to correct image noise background due to the

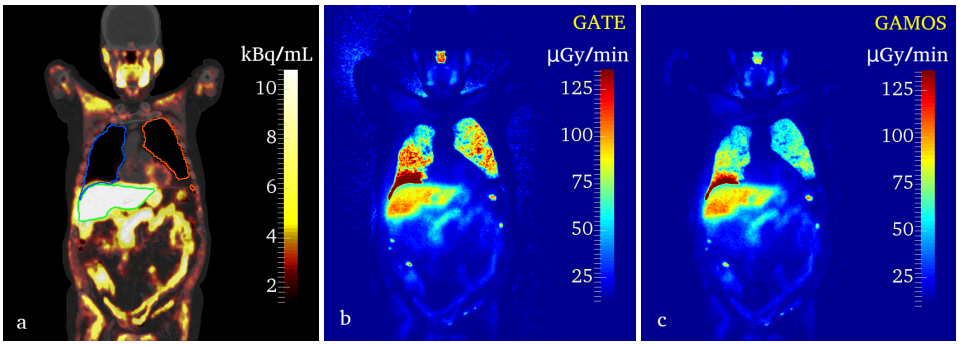

FIGURE 2. CT and ^{18}F-choline PET fusion of coronal slices (a) with VOIs contours (green: liver, blue: right lung, orange: left lung); corresponding coronal slices of dose rate (μGy/min) maps estimated respectively with GATE (b) and GAMOS (c) simulations.

PET image reconstruction process, whereas other sources of spurious emission were not corrected (*i.e.*, misalignment of PET and CT scans and patient or organ movements). Since the event generation probability distribution is built from the PET scan, a non-zero event generation probability will be associated to voxels having noise-induced non-zero activity concentration in the PET. In these noisy areas an erroneous dose rate background could be evaluated through MC simulations. To quantify this contribution, we performed further simulations using, as input data for the source distribution, the PET scan filtered through the procedure described in the following. Firstly, by means of 3DSlicer modules, we set to zero all the PET scan voxels corresponding to CT voxels to whom air is assigned as material, thus with HU< -855 (Table 2). Then we applied a threshold filter setting to zero all the PET voxels with activity less than 100 Bq/mL. This cut was chosen in order to avoid decay generation in areas outside the patient not identified as air - because of their slightly higher density - but improperly identified as lung tissue (mainly the PET/CT bed and some PET reconstruction artifacts near it) by GATE and GAMOS materials assignment procedures previously described. Aim of all this procedure was to minimize the probability of generating decays in areas actually corresponding to air, inside and outside the patient body, and to materials not belonging to the patient body.

The "filtered-PET" simulations were carried out using all the same macros and settings adopted for the "unfiltered-PET" simulations, the only difference being the input image. The same types of outputs were deduced: dose rate maps, dose-rate average values into VOIs, DVRHs. Referring to Eq. 1, in the case of filtered-PET $A(t_s)$ is retrieved as well from the native PET. The overall procedure therefore ensures the conservation of the total rate of decays.

The average dose rate results are presented for each VOI, accompanied by their corresponding *average* statistical uncertainties δ (%), deduced with 3DSlicer *Segment Statistics* starting from MC simulation generated relative uncertainty maps. We set 10^8 as the number of generated events in the simulations (N_{evts}), that ensured in both unfiltered- and filtered-PET simulations a mean statistical uncertainty of dose evaluation below 6% in the liver

TABLE 4. Average absorbed dose rates $\langle \dot{D} \rangle$ to VOIs and corresponding mean statistical uncertainties δ. Comparison between GATE and GAMOS results is presented through ε (Eq. 3) and $\langle \varepsilon_{ijk} \rangle$ (Eq. 4).

VOI	Liver	Right Lung	Left Lung
Volume (cc)	1074	2091	1797
$\langle \dot{D} \rangle_{\text{GATE}}$ (μGy/min)	83.34	71.42	59.79
δ_{GATE} (%)	$\pm$5.55	$\pm$14.55	$\pm$15.60
$\langle \dot{D} \rangle_{\text{GAMOS}}$ (μGy/min)	84.28	62.74	50.67
δ_{GAMOS} (%)	$\pm$5.55	$\pm$13.20	$\pm$14.28
ε (%)	$-$1.11	+13.83	+18.01
$\langle \varepsilon_{ijk} \rangle$ (%)	$-$0.44	+12.83	+17.26

VOI. The comparison between GATE and GAMOS average dose rate values, both for the unfiltered- and filtered-PET simulations, is presented for each VOI in terms of relative per cent difference ε (%), taking GAMOS as a reference:

$$\varepsilon = \frac{\langle \dot{D}^{\,\text{GATE}}(t_s) \rangle - \langle \dot{D}^{\,\text{GAMOS}}(t_s) \rangle}{\langle \dot{D}^{\,\text{GAMOS}}(t_s) \rangle} \cdot 100 \tag{3}$$

We furthermore compared GATE and GAMOS dose rates evaluating their relative percent difference for each voxel (i, j, k), ε_{ijk} (%):

$$\varepsilon_{ijk} = \frac{\dot{D}_{ijk}^{\text{GATE}}(t_s) - \dot{D}_{ijk}^{\text{GAMOS}}(t_s)}{\dot{D}_{ijk}^{\text{GAMOS}}(t_s)} \cdot 100 \tag{4}$$

and their average value $\langle \varepsilon_{ijk} \rangle$ (%) in VOIs. The comparison between unfiltered- and filtered-PET average dose rate values is presented in terms of their relative per cent difference κ (%), taking the unfiltered ones as a reference:

$$\kappa = \frac{\langle \dot{D}^{\,\text{fil}}(t_s) \rangle - \langle \dot{D}^{\,\text{unfil}}(t_s) \rangle}{\langle \dot{D}^{\,\text{unfil}}(t_s) \rangle} \cdot 100 \tag{5}$$

3. Results and discussion

Considering first the results of the simulations employing the native unfiltered PET scan, a couple of coronal dose rate map are shown in Fig. 2, in panel (b) obtained with GATE and in panel (c) with GAMOS. In Table 4 we report the average absorbed dose rates to the defined VOIs and the relative per cent differences between GATE and GAMOS results. A very good agreement, within about 1% considering ε, was found for the liver VOI, while concerning both lung VOIs wider differences were observed, with GATE overestimating dose rates in lungs with respect to GAMOS; nevertheless the agreement is acceptable, since differences fall within the dose rates mean statistical uncertainties δ. A fair agreement is found also considering the voxel-by-voxel dose rate differences, ε_{ijk}, whose distributions in VOIs are reported in Fig. 3 (panels (a), (c), (e)) and whose average values $\langle \varepsilon_{ijk} \rangle$ are

TABLE 5. Dose rate average values, δ, ε, $\langle \varepsilon_{ijk} \rangle$ and κ, as described in Sect. 2.

VOI	Liver	Right Lung	Left Lung
Volume (cc)	1074	2091	1797
$\langle \dot{D} \rangle_{\mathrm{GATE_{fil}}}$ (μGy/min)	86.27	38.36	28.55
$\delta_{\mathrm{GATE_{fil}}}$ (%)	$\pm$5.63	$\pm$19.80	$\pm$22.21
$\langle \dot{D} \rangle_{\mathrm{GAMOS_{fil}}}$ (μGy/min)	86.82	37.38	26.96
$\delta_{\mathrm{GAMOS_{fil}}}$ (%)	$\pm$5.62	$\pm$17.72	$\pm$20.21
$\varepsilon_{\mathrm{fil}}$ (%)	$-$0.64	+2.60	+5.91
$\langle \varepsilon_{ijk} \rangle_{\mathrm{fil}}$ (%)	$-$0.40	+9.40	+14.66
κ_{GATE} (%)	+3.51	$-$46.29	$-$52.25
κ_{GAMOS} (%)	+3.02	$-$40.42	$-$46.80

comparable with ε values and fall within δ values. The statistical uncertainties in lungs are larger with respect to the ones in liver, due to the heterogeneous composition of lungs, mainly containing lung tissue and air. Having lower average density and thus lower interaction probabilities with radiation than soft tissue, less interactions happen and are simulated in these regions; therefore larger statistical uncertainties are associated to absorbed doses inside them. The larger differences in lungs dose rates between GATE and GAMOS compared to the ones for liver are attributable to the different procedure the two toolkits employ to assign densities in voxels. A different assignment of density value appears to have more impact for low density voxels (lungs), causing wider mean differences in their dose outcomes than in more dense voxels (liver).

Observing the dose rate maps (see Figs. 2(b) and 2(c)), it can be noticed that a certain amount of background dose rate outside the patient shape is present. It is partly due to the interactions of the annihilation photons with the air and materials outside the patient. However it must be attributed partly also to the ^{18}F decays generated outside the patient body by the simulation because of noise-induced non-zero activity concentration distributions outside the patient body in the PET data. High dose rate distributions and spots can be observed from the dose rate maps (some of them visible in Fig. 2(b) and 2(c)) in correspondence of areas inside the patient body containing air: oro-nasal cavity, larynx, trachea, esophagus, stomach and intestinal tracts, and especially lungs. Given these evidences, it can be hypothesized that decays generated "erroneously" in air, both outside and inside the patient phantom, may influence the absorbed dose rate evaluation, possibly causing dose artifacts and overestimation in certain anatomical regions.

The average dose rate results obtained with the simulations carried out using the filtered PET are reported in Table 5 and compared with the results coming from the native PET (Table 4). A slight increase, of about 3% (κ), of the average dose rate in liver is observed with both MC codes, when using the filtered PET. Instead, a 40% up to 50% decrease of average dose rate is observed for lungs, still for both GATE and GAMOS. These differences are not merely imputable to statistical fluctuations, because their magnitude largely exceeds the - albeit significant - mean statistical uncertainties δ_{fil}. This lowering of dose rate with respect to the unfiltered-PET simulation can be appreciated visually in Fig. 4, showing dose

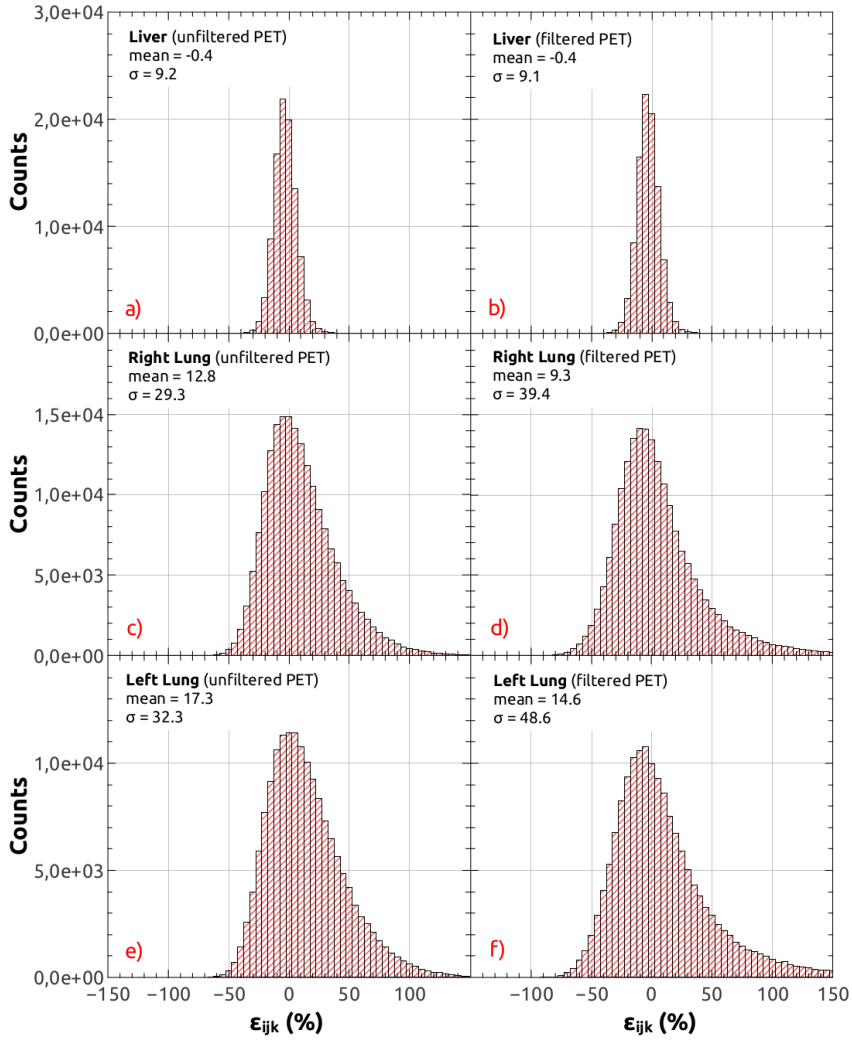

FIGURE 3. Distributions of dose rate relative percent difference at voxel level, ε_{ijk}, in the defined VOIs for unfiltered (panels a, c, e) and filtered (panels b, d, f) PET simulations.

rate map slices (fused with CT slices to have a clearer morphological reference) obtained with unfiltered- and filtered-PET GATE simulations and the voxel-by-voxel differences between the two maps.

A reduction up to about half and beyond of the unfiltered values can be seen in lungs as well as in other spots in oral cavity and abdomen, and a lowering of the background outside the patient body is observed. Looking at panels (b2) and (c2) of Fig. 4 compared to panels (b1) and (c1), it can be seen that, despite an almost general decrease in the right lung

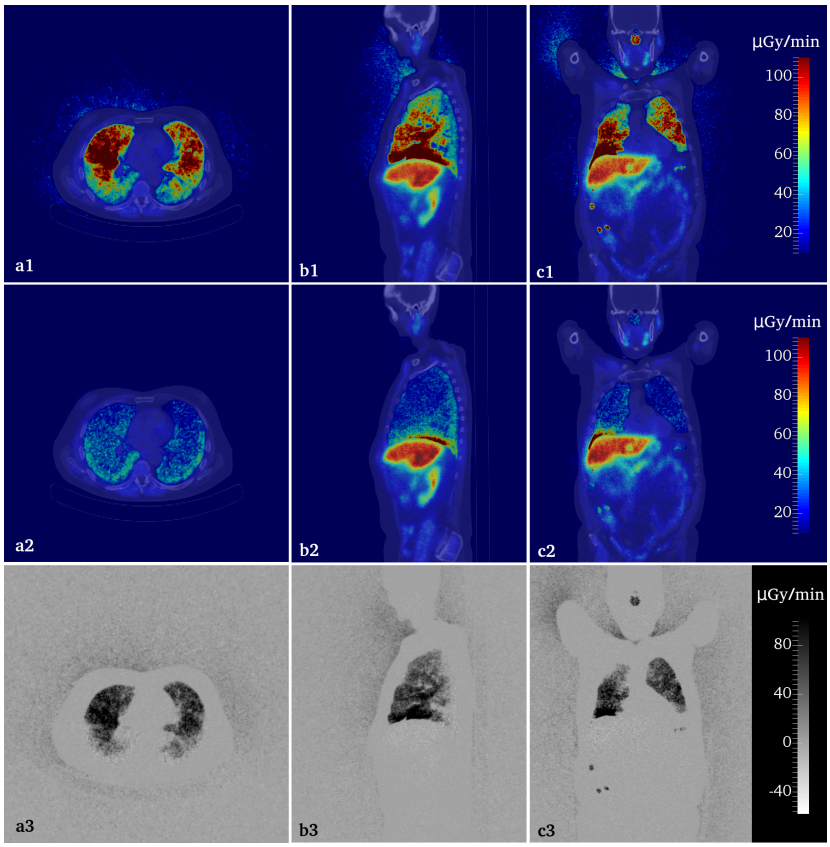

FIGURE 4. Axial, sagittal and coronal slices of dose rate maps estimated with GATE using original PET (a1, b1, c1) and filtered PET (a2, b2, c2) as input data, and the corresponding slices obtained subtracting voxel-by-voxel the filtered dose map from the original one (a3, b3, c3).

dose rate, in its lower part high dose rate distribution remains. Part of it is reasonably and realistically caused by energy deposition coming from decays generated in the simulation in perfused lower lung itself and from perfused liver. However another part is likely due to decays generated in the simulation in the lower part of the right lung, but generated there because of event decay probability actually due to liver activity accidentally measured in the lower lung, as a consequence of the respiratory motion during the PET acquisition (Pépin *et al.* 2014). This spill-out of the liver activity can be seen in Fig. 2(a). It is evident how the filtering procedure adopted is unable to correct for this kind of artifact.

From the comparison between GATE and GAMOS filtered-PET dose rate results (Table 5), an agreement within 6% considering $\varepsilon_{\mathrm{fil}}$ is present in all considered VOIs, that is below the mean statistical uncertainties δ_{fil}. As regards $\langle \varepsilon_{ijk} \rangle_{\mathrm{fil}}$ parameter, we get an agreement within 15% in all considered VOIs; $\varepsilon_{ijk\,\mathrm{fil}}$ distributions are shown in Fig. 3 (panels (b), (d), (f)).

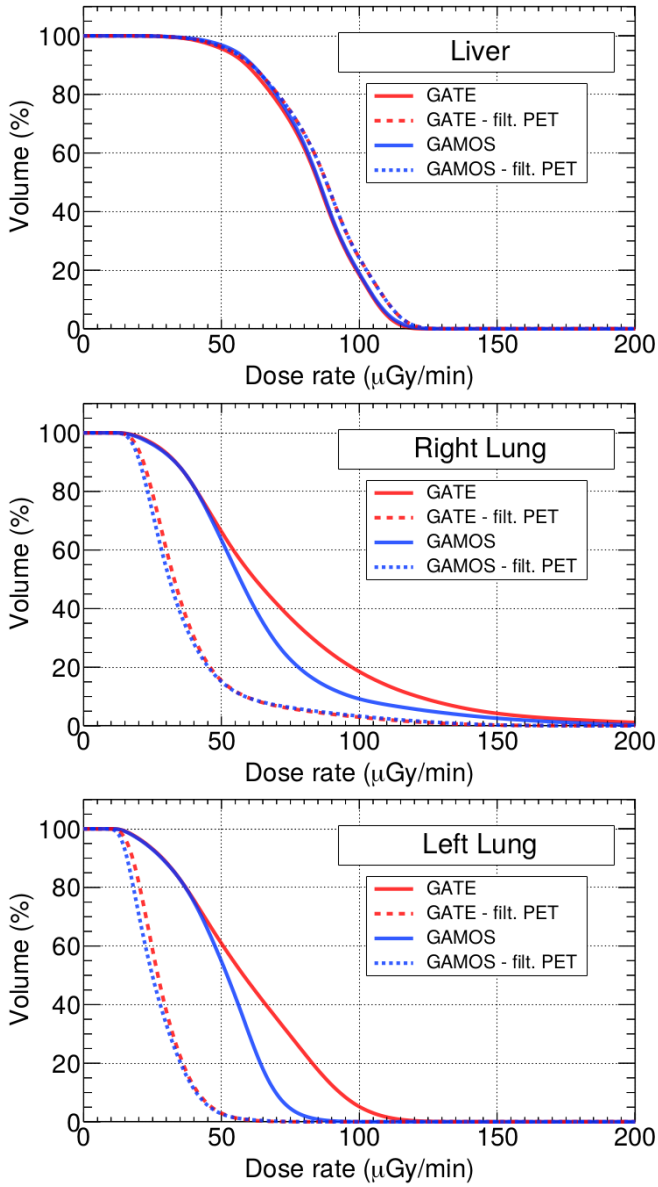

FIGURE 5. DRVHs in the defined VOIs. Solid lines are relative to unfiltered-PET simulations, dotted lines to filtered-PET simulations.

These evidences can be further appreciated looking at the DRVHs in Fig. 5, reported for both unfiltered- and filtered-PET simulations. From lungs DRVHs it can be observed that, while for the unfiltered-PET simulations there is a certain difference in dose rates in less

than the 60% of the volume, for the filtered-PET simulations there is an excellent agreement between GATE and GAMOS. This evidence supports the supposition that the differences between GATE and GAMOS results built on unfiltered PET, also emerging in Table 4, could be due to the different density assignment procedures, having a stronger influence on low density voxels. Indeed the minimization of decay generation in low density voxels, obtained through PET filtering, causes a reduction of the contribution of low density voxels to the dose rate; their "exclusion" in filtered PET brings GATE and GAMOS simulations to find closer agreement. Concerning liver, GATE and GAMOS DVRHs show excellent agreement for both unfiltered- and filtered-PET cases, in agreement with the hypothesis of higher density voxels being less influenced by differences in the density assignment procedures.

The previously highlighted significant decrease of lungs dose rate in filtered-PET simulations with respect to the unfiltered-PET ones clearly appears also in DRVHs. Likewise it is observable the slight increase of liver dose rate in filtered-PET simulations. It can be justified by the filter-caused reduction of decay generation in air-associated areas and, being equal the number of generated events, the consequent enhancement of decays in all other non-zero activity areas.

Based on the obtained results, we can deduce that the unfiltered-PET simulations generate a significant amount of decays in the air inside lungs and some other anatomical districts, enough to cause a considerable overestimation of absorbed dose rate with respect to the filtered-PET simulations. Filtered-PET simulations could better reproduce a more realistic scenario in which the absorbed dose rates to organs like lungs, with a substantial presence of air inside them, and to the body external surface, are solely due to decays happening in perfused tissues and not improperly in air.

4. Conclusions

A comparison was made between the dosimetric results obtained with GATE and GAMOS MC simulations of a routinary PET exam employing ^{18}F-choline. 3D absorbed dose rate maps and DRVHs in VOIs corresponding to liver and lungs were produced. The results obtained for liver were in very good agreement, with relative differences of about 1%. A much lower but still acceptable agreement was found for lungs, presumably due to the different voxel density assignment procedure. A PET filtering technique, with the aim of minimizing decay generation in air and in materials outside the patient volume, was implemented in order to investigate and quantify dose rate artifacts and overestimations due to PET background. A dose rate decrease of about 40% was observed in lungs for filtered-PET simulations with respect to the unfiltered ones. Regarding the liver, a very slight dose rate increase of about 3% was observed. A general lowering of background and high-dose-spots corresponding to air-rich regions was also obtained. An excellent agreement between GATE and GAMOS was found for the filtered results in all VOIs, within 6% in all of them and in particular within less than 1% in liver, supporting the hypothesis of density assignment procedures differences having more influence on low density voxels.

References

3DSlicer (2020). 3DSlicer User Manual Documentation. URL: https://www.slicer.org/wiki/Documentation/4.10 (visited on 01/29/2020).

Agostinelli, S., Allison, J., Amako, K., Apostolakis, J., Araujo, H., Arce, P., Asai, M., Axen, D., Banerjee, S., Barrand, G., Behner, F., Bellagamba, L., Boudreau, J., Broglia, L., Brunengo, A., Burkhardt, H., Chauvie, S., Chuma, J., Chytracek, R., Cooperman, G., Cosmo, G., Degtyarenko, P., Dell'Acqua, A., Depaola, G., Dietrich, D., Enami, R., Feliciello, A., Ferguson, C., Fesefeldt, H., Folger, G., Foppiano, F., Forti, A., Garelli, S., Giani, S., Giannitrapani, R., Gibin, D., Gómez Cadenas, J. J., González, I., Gracia Abril, G., Greeniaus, G., Greiner, W., Grichine, V., Grossheim, A., Guatelli, S., Gumplinger, P., Hamatsu, R., Hashimoto, K., Hasui, H., Heikkinen, A., Howard, A., Ivanchenko, V., Johnson, A., Jones, F. W., Kallenbach, J., Kanaya, N., Kawabata, M., Kawabata, Y., Kawaguti, M., Kelner, S., Kent, P., Kimura, A., Kodama, T., Kokoulin, R., Kossov, M., Kurashige, H., Lamanna, E., Lampén, T., Lara, V., Lefebure, V., Lei, F., Liendl, M., Lockman, W., Longo, F., Magni, S., Maire, M., Medernach, E., Minamimoto, K., Mora de Freitas, P., Morita, Y., Murakami, K., Nagamatu, M., Nartallo, R., Nieminen, P., Nishimura, T., Ohtsubo, K., Okamura, M., O'Neale, S., Oohata, Y., Paech, K., Perl, J., Pfeiffer, A., Pia, M. G., Ranjard, F., Rybin, A., Sadilov, S., Di Salvo, E., Santin, G., Sasaki, T., Savvas, N., Sawada, Y., Scherer, S., Sei, S., Sirotenko, V., Smith, D., Starkov, N., Stoecker, H., Sulkimo, J., Takahata, M., Tanaka, S., Tcherniaev, E., Safai Tehrani, E., Tropeano, M., Truscott, P., Uno, H., Urban, L., Urban, P., Verderi, M., Walkden, A., Wander, W., Weber, H., Wellisch, J. P., Wenaus, T., Williams, D. C., Wright, D., Yamada, T., Yoshida, H., and Zschiesche, D. (2003). "Geant4 - a simulation toolkit". *Nuclear Instruments and Methods in Physics Research Section A: Accelerators, Spectrometers, Detectors and Associated Equipment* **506**(3), 250–303. DOI: 10.1016/S0168-9002(03)01368-8.

Allison, J., Amako, K., Apostolakis, J., Arce, P., Asai, M., Aso, T., Bagli, E., Bagulya, A., Banerjee, S., Barrand, G., Beck, B. R., Bogdanov, A. G., Brandt, D., Brown, J. M. C., Burkhardt, H., Canal, P., Cano-Ott, D., Chauvie, S., Cho, K., Cirrone, G. A. P., Cooperman, G., Cortés-Giraldo, M. A., Cosmo, G., Cuttone, G., Depaola, G., Desorgher, L., Dong, X., Dotti, A., Elvira, V. D., Folger, G., Francis, Z., Galoyan, A., Garnier, L., Gayer, M., Genser, K. L., Grichine, V. M., Guatelli, S., Guèye, P., Gumplinger, P., Howard, A. S., Hřivnáčová, I., Hwang, S., Incerti, S., Ivanchenko, A., Ivanchenko, V. N., Jones, F. W., Jun, S. Y., Kaitaniemi, P., Karakatsanis, N., Karamitros, M., Kelsey, M., Kimura, A., Koi, T., Kurashige, H., Lechner, A., Lee, S. B., Longo, F., Maire, M., Mancusi, D., Mantero, A., Mendoza, E., Morgan, B., Murakami, K., Nikitina, T., Pandola, L., Paprocki, P., Perl, J., Petrović, I., Pia, M. G., Pokorski, W., Quesada, J. M., Raine, M., Reis, M. A., Ribon, A., Ristić Fira, A., Romano, F., Russo, G., Santin, G., Sasaki, T., Sawkey, D., Shin, J. I., Strakovsky, I. I., Taborda, A., Tanaka, S., Tomé, B., Toshito, T., Tran, H. N., Truscott, P. R., Urban, L., Uzhinsky, V., Verbeke, J. M., Verderi, M., Wendt, B. L., Wenzel, H., Wright, D. H., Wright, D. M., Yamashita, T., Yarba, J., and Yoshida, H. (2016). "Recent developments in Geant4". *Nuclear Instruments and Methods in Physics Research Section A: Accelerators, Spectrometers, Detectors and Associated Equipment* **835**, 186–225. DOI: 10.1016/j.nima.2016.06.125.

Amato, E., Cicone, F., Auditore, L., Baldari, S., Prior, J., and Gnesin, S. (2018). "A Monte Carlo model for the internal dosimetry of choroid plexuses in nuclear medicine procedures". *Physica Medica: European Journal of Medical Physics* **49**, 52–57. DOI: 10.1016/j.ejmp.2018.05.005.

Amato, E., Italiano, A., and Baldari, S. (2013a). "Monte Carlo study of voxel S factor dependence on tissue density and atomic composition". *Nuclear Instruments and Methods in Physics Research Section A: Accelerators, Spectrometers, Detectors and Associated Equipment* **729**, 870–876. DOI: 10.1016/j.nima.2013.08.059.

Amato, E., Italiano, A., Minutoli, F., and Baldari, S. (2013b). "Use of the GEANT4 Monte Carlo to determine three-dimensional dose factors for radionuclide dosimetry". *Nuclear Instruments and*

Methods in Physics Research Section A: Accelerators, Spectrometers, Detectors and Associated Equipment **708**, 15–18. DOI: 10.1016/j.nima.2013.01.014.

Amato, E., Minutoli, F., Pacilio, M., Campennì, A., and Baldari, S. (2012). "An analytical method for computing voxel S values for electrons and photons". *Medical Physics* **39**(11), 6808–6817. DOI: 10.1118/1.4757912.

Arce, P., Rato, P., Canadas, M., and Lagares, J. I. (2008). "GAMOS: A Geant4-based easy and flexible framework for nuclear medicine applications". *2008 IEEE Nuclear Science Symposium Conference Record*, 3162–3168. DOI: 10.1109/NSSMIC.2008.4775023.

Auditore, L., Amato, E., Italiano, A., Arce, P., Campennì, A., and Baldari, S. (2019). "Internal dosimetry for TARE therapies by means of GAMOS Monte Carlo simulations". *Physica Medica: European Journal of Medical Physics* **64**, 245–251. DOI: 10.1016/j.ejmp.2019.07.024.

Bolch, W. E., Bouchet, L. G., Robertson, J. S., Wessels, B. W., Siegel, J. A., Howell, R. W., Erdi, A. K., Aydogan, B., Costes, S., and Watson, E. E. (1999). "MIRD pamphlet No. 17: the dosimetry of nonuniform activity distributions: radionuclide S values at the voxel level". *The Journal of Nuclear Medicine* **40**(1), 11S–36S. URL: http://jnm.snmjournals.org/content/40/1/11S.short. [In collaboration with the MIRD Committee, Society of Nuclear Medicine: E. E. Watson (Chair), J. S. Robertson (Task Group Leader), W. E. Bolch, A. B. Brill, N. D. Charkes, D. R. Fisher, M. T. Hays, R. W. Howell, J. A. Siegel, S. R. Thomas and B. W. Wessels].

Dewaraja, Y. K., Frey, E. C., Sgouros, G., Brill, A. B., Roberson, P., Zanzonico, P. B., and Ljungberg, M. (2012). "MIRD pamphlet No. 23: quantitative SPECT for patient-specific 3-dimensional dosimetry in internal radionuclide therapy". *The Journal of Nuclear Medicine* **53**(8), 1310–1325. DOI: 10.2967/jnumed.111.100123.

GAMOS (2020). GAMOS User's Guide. URL: http://fismed.ciemat.es/GAMOS/GAMOS_doc/GAMOS.6.0.0/GamosUsersGuide_V6.0.0.html (visited on 01/29/2020).

GATE (2020). GATE User's Guide. URL: https://opengate.readthedocs.io/en/latest/ (visited on 01/29/2020).

Geant4 (2020). Geant4 Physics Reference Manual. URL: http://geant4-userdoc.web.cern.ch/geant4-userdoc/UsersGuides/PhysicsReferenceManual/html/index.html (visited on 01/29/2020).

Giap, H. B., Macey, D. J., Bayouth, J. E., and Boyer, A. L. (1995). "Validation of a dose-point kernel convolution technique for internal dosimetry". *Physics in Medicine & Biology* **40**(3), 365–381. DOI: 10.1088/0031-9155/40/3/003.

Jacobson, O., Kiesewetter, D. O., and Chen, X. (2015). "Fluorine-18 radiochemistry, labeling strategies and synthetic routes". *Bioconjugate Chemistry* **26**(1), 1–18. DOI: 10.1021/bc500475e.

Jadvar, H. (2012). "Molecular imaging of prostate cancer: PET radiotracers". *American Journal of Roentgenology* **199**(2), 278–291. DOI: 10.2214/AJR.12.8816.

Jan, S., Santin, G., Strul, D., Staelens, S., Assié, K., Autret, D., Avner, S., Barbier, R., Bardiès, M., Bloomfield, P. M., Brasse, D., Breton, V., Bruyndonckx, P., Buvat, I., Chatziioannou, A. F., Choi, Y., Chung, Y. H., Comtat, C., Donnarieix, D., Ferrer, L., Glick, S. J., Groiselle, C. J., Guez, D., Honore, P.-F., Kerhoas-Cavata, S., Kirov, A. S., Kohli, V., Koole, M., Krieguer, M., Laan, D. J. van der, Lamare, F., Largeron, G., Lartizien, C., Lazaro, D., Maas, M. C., Maigne, L., Mayet, F., Melot, F., Merheb, C., Pennacchio, E., Perez, J., Pietrzyk, U., Rannou, F. R., Rey, M., Schaart, D. R., Schmidtlein, C. R., Simon, L., Song, T. Y., Vieira, J.-M., Visvikis, D., Walle, R. V. de, Wieërs, E., and Morel, C. (2004). "GATE: a simulation toolkit for PET and SPECT". *Physics in Medicine & Biology* **49**(19), 4543–4561. DOI: 10.1088/0031-9155/49/19/007.

Pépin, A., Daouk, J., Bailly, P., Hapdey, S., and Meyer, M.-E. (2014). "Management of respiratory motion in PET/computed tomography: the state of the art". *Nuclear Medicine Communications* **35**(2), 113–122. DOI: 10.1097/MNM.0000000000000048.

Sarrut, D., Bardiès, M., Boussion, N., Freud, N., Jan, S., Létang, J.-M., Loudos, G., Maigne, L., Marcatili, S., Mauxion, T., Papadimitroulas, P., Perrot, Y., Pietrzyk, U., Robert, C., Schaart, D. R.,

Visvikis, D., and Buvat, I. (2014). "A review of the use and potential of the GATE Monte Carlo simulation code for radiation therapy and dosimetry applications". *Medical Physics* **41**(6), 064301. DOI: 10.1118/1.4871617.

Stokke, C., Gabiña, P. M., Solný, P., Cicone, F., Sandström, M., Gleisner, K. S., Chiesa, C., Spezi, E., Paphiti, M., Konijnenberg, M., Aldridge, M., Tipping, J., Wissmeyer, M., Brans, B., Bacher, K., Kobe, C., and Flux, G. (2017). "Dosimetry-based treatment planning for molecular radiotherapy: a summary of the 2017 report from the Internal Dosimetry Task Force". *European Journal of Nuclear Medicine and Molecular Imaging Physics* **4**, 27. DOI: 10.1186/s40658-017-0194-3.

---

[a] Università degli Studi di Messina
Dipartimento di Scienze Matematiche e Informatiche, Scienze Fisiche e Scienze della Terra
Contrada Papardo, 98166 Messina, Italy

[b] Istituto Nazionale di Fisica Nucleare
Sezione di Catania, Catania, Italy

[c] Università degli Studi di Messina
Dipartimento di Scienze Biomediche, Odontoiatriche e delle Immagini Morfologiche e Funzionali
Sezione di Scienze Radiologiche
Via Consolare Valeria, 98125 Messina, Italy

[d] Azienda Ospedaliera Universitaria Policlinico "G. Martino"
Unità di Medicina Nucleare
Via Consolare Valeria, 98125 Messina, Italy

[*] To whom correspondence should be addressed | email: italianoa@unime.it

Communicated 3 December 2019; manuscript received 3 February 2020; published online 27 May 2020